INTERNATIONAL JOURNAL OF
Minerals, Metallurgy and Materials

Volume 31, Number 7, July 2024
Page 1525

Research Article https://doi.org/10.1007/s12613-024-2905-9

Evolution of nonmetallic inclusions in 80-t 9CrMoCoB large-scale ingots during electroslag remelting process

Shengchao Duan[1,2], *Min Joo Lee*[2], *Yao Su*[2], *Wangzhong Mu*[3,4], *Dong Soo Kim*[5], *and Joo Hyun Park*[2],✉

1) School of Mechanical and Materials Engineering, North China University of Technology, Beijing 100144, China
2) Department of Materials Science and Chemical Engineering, Hanyang University, Ansan 15588, Rep. of Korea
3) Department of Materials Science and Engineering, KTH Royal Institute of Technology, Brinellvägen 23, Stockholm 10044, Sweden
4) Department of Engineering Science and Mathematics, Division of Materials Science, Luleå University of Technology, 97187 Luleå, Sweden
5) Casting & Forging Business Unit, Nuclear Business Group, Doosan Enerbility, Changwon 51711, Rep. of Korea

(Received: 16 October 2023; revised: 4 April 2024; accepted: 7 April 2024)

Abstract: In combination with theoretical calculations, experiments were conducted to investigate the evolution behavior of nonmetallic inclusions (NMIs) during the manufacture of large-scale heat-resistant steel ingots using 9CrMoCoB heat-resistant steel and CaF_2–CaO–Al_2O_3–SiO_2–B_2O_3 electroslag remelting (ESR)-type slag in an 80-t industrial ESR furnace. The main types of NMI in the consumable electrode comprised pure alumina, a multiphase oxide consisting of an Al_2O_3 core and liquid CaO–Al_2O_3–SiO_2–MnO shell, and $M_{23}C_6$ carbides with an MnS core. The Al_2O_3 and MnS inclusions had higher precipitation temperatures than the $M_{23}C_6$-type carbide under equilibrium and nonequilibrium solidification processes. Therefore, inclusions can act as nucleation sites for carbide layer precipitation. The ESR process completely removed the liquid CaO–Al_2O_3–SiO_2–MnO oxide and MnS inclusion with a carbide shell, and only the Al_2O_3 inclusions and Al_2O_3 core with a carbide shell occupied the remelted ingot. The $M_{23}C_6$-type carbides in steel were determined as $Cr_{23}C_6$ based on the analysis of transmission electron microscopy results. The substitution of Cr with W, Fe, or/and Mo in the $Cr_{23}C_6$ lattice caused slight changes in the lattice parameter of the $Cr_{23}C_6$ carbide. Therefore, $Cr_{21.34}Fe_{1.66}C_6$, $(Cr_{19}W_4)C_6$, $Cr_{18.4}Mo_{4.6}C_6$, and $Cr_{16}Fe_5Mo_2C_6$ can match the fraction pattern of $Cr_{23}C_6$ carbide. The Al_2O_3 inclusions in the remelted ingot formed due to the reduction of CaO, SiO_2, and MnO components in the liquid inclusion. The increased Al content in liquid steel or the higher supersaturation degree of Al_2O_3 precipitation in the remelted ingot than that in the electrode can be attributed to the evaporation of CaF_2 and the increase in CaO content in the ESR-type slag.

Keywords: nonmetallic inclusion; heat-resistant steel; electroslag remelting; $M_{23}C_6$ carbide; MnS inclusion; supersaturation degree

1. Introduction

Heat-resistant steels containing 9wt% to 12wt% Cr have been widely used in high-efficiency ultrasupercritical power plants for the reduction of greenhouse gas emissions, given their favorable mechanical properties in extreme environments and at an elevated temperature of around 923 K (e.g., good oxidation resistance, high creep strength, and optimum thermal fatigue properties) [1–3]. However, $M_{23}C_6$ carbides experience coarsening during long-term service at high operating temperatures, which can deteriorate the creep strength of heat-resistant steel [4–7]. The addition of the 0.005wt%–0.01wt% alloying element boron (B) can retard the coarsening rate of $M_{23}C_6$ carbides and refine grains in 9CrMoCoB steel, which further improves the abovementioned mechanical properties [8–10]. The addition of boron usually follows the deoxidation and degassing of liquid steel in the form of a complex ferroalloy with certain amounts of Al and Ti to prevent the formation of BN and B_2O_3 [10]. Adjustment on the activity of B_2O_3 in the slag system alleviates the oxidation loss of B in ingots resulting from redox reactions at the slag/metal interface [11–14].

On the other hand, the presence of nonmetallic inclusion (NMI) poses harm to the manufacture of steels and alloys and generates various defects in alloy products [15–17]. Some researchers have observed various types of NMIs in Ni–Fe-based superalloys [18–20], such as oxides [21–23], carbides [24–26], carbonitrides [27–28], sulphocarbide [29–30], and complex inclusions [31–33]. Studies have also reported the NMIs in heat-resistant steel with high-Cr content [34–36]. Sakuraya *et al.* [34] revealed the formation of BN inclusions in high-Cr ferritic heat-resistant steel with 0.001wt% B and 0.015wt% N and their complete dissolution in a steel matrix at 1523 K. Li *et al.* [35] investigated the evolution of oxide inclusions in 253 MA heat-resistant steel (21Cr–11Ni–0.04Ce, wt%) deoxidized by Si–Al alloy at the temperature range of 1773 to 1873 K. They observed that the liquid Ce–Si–Al–O system inclusions in steel eliminated nozzle

---

✉ Corresponding author: Joo Hyun Park E-mail: basicity@hanyang.ac.kr

clogging of Ce-containing steel. Zhang *et al.* [36] examined the effect of electromagnetic stirring on the cleanliness of Fe–18Cr–2Ni–1Mo–0.2C–0.2Mn–0.1Si (wt%) heat-resistant steels containing 3%–12% Co. They observed two main types of inclusions, namely, Al_2O_3 and $MnO{\cdot}Cr_2O_3$ spinel, generated in the solidification process and the decreased density and size of inclusions after electromagnetic stirring (EMS) treatment.

To reduce the amount of harmful NMIs and obtain a superior solidification structure, scholars have adopted electroslag remelting (ESR) to manufacture high-quality steels and alloys [37–39]. Experimental and numerical research has focused on the removal behavior of NMIs in various steel grades during the ESR process [40–44]. However, fundamental studies on the ESR of heat-resistant steel are limited. Wang *et al.* [45] conducted laboratory-scale experiments and reported the transformation of the initial $MnO–SiO_2–Al_2O_3–CaO$ system inclusions in the steel electrode into Al_2O_3 and $CaO–Al_2O_3$ inclusions in the liquid-metal pool and remelted ingots. Zhao *et al.* [46] researched the evolution of inclusions in Ce-containing heat-resistant steel during protective-atmosphere ESR. They stated the presence of Ce_2O_2S and Ce_2O_3 inclusions in the consumable electrode, liquid-metal pool, and remelted ingot, which indicates that the inclusions were unremovable during the ESR process.

To the best of the present authors' knowledge, no study has reported the evolution of inclusions during the manufacture of a large 9CrMoCoB ingot. In the present study, an industrial experiment was conducted on an 80-t industrial ESR furnace to investigate the differences in the inclusions, including oxides, sulfides, and carbides, at various locations in the electrode and remelted ingot to provide assistance in the production of large 9CrMoCoB ingots with high cleanness.

2. Experimental

9CrMoCoB steel (1600 mm in diameter) was served as the consumable electrode. The manufacture of the ESR electrode was completed in a 100-t electrical arc furnace and ladle furnace (LF). Table 1 lists the chemical composition of the electrodes. Oxidation loss of major alloy elements, such as Si, Mn, Nb, and B, was prevented by controlling the oxygen content in the mold below 0.1wt%. An industrial experiment was performed in an industrial 80-t–scale ESR furnace (melting capacity: 150 t; Consarc, USA). Table 2 provides the operating parameters of the ESR process. The introduction of high-purity Ar gas (the contents of impurity components, such as H_2O, oxygen, nitrogen, and hydrogen, were less than 1 ppm) into the chamber of the ESR furnace resulted in the isolation of the air atmosphere and oxidation loss of the reactive element, i.e., B, during the ESR process. The 9CrMoCoB steel electrode (diameter: 1600 mm and weight: 80 t) was refined using $CaF_2–CaO–Al_2O_3–SiO_2–B_2O_3$ slag (masss ratio of $B_2O_3/SiO_2 = 0.04$); the design approach to slag composition for the control of the homogenous distribution of B in a large 9CrMoCoB ingot has been described elsewhere [14]. The variations in SiO_2 and B_2O_3 contents in $CaF_2–CaO–Al_2O_3–SiO_2–B_2O_3$ slag have been verified via effective strategies to control the oxidation of alloying elements Si and B in the ESR ingot.

Table 1. Chemical compositions of 9CrMoCoB steel wt%

C	Si	Mn	S	Cr	B	Al	O	Others*	Fe
0.13	0.08	0.08	0.003	10.2	0.003	0.004	0.003	5.7	Bal.

Note: *Ni + Mo+ V + W + Co.

Table 2. Parameters for the electroslag remelting of 9CrMoCoB steel

Start method	Voltage swing / V	Remelting current / kA	Atmosphere	Fill ratio
Cold start	8–10	65	Ar	0.7

After the experiment, four metal samples were collected from the top and bottom parts of the remelted ingot (diameter: 2150 mm), with two samples being further obtained from the center and surface of each part. The sampling positions in the remelted ingot corresponded to various refinement stages, with the bottom and top parts representing the initial and final stages of the ESR process, respectively. Fig. 1 shows the external shape and appearance of the remelted ingot.

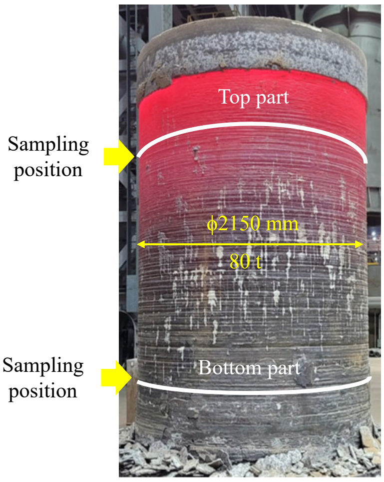

Fig. 1. External shape of the remelted steel ingot.

To investigate the morphology of NMI in two-dimensional (2D) alloy, pieces of the metal sample were resin-mounted and ground with 2000-grade SiC paper. Surface finishing was conducted on a polishing machine using a 1 μm polycrystalline diamond suspension. 2D observations revealed imprecise compositions of inclusions, which were due to the excitation effect of the matrix phase. Hence, three-dimensional (3D) observations were performed after electrolytic extraction to observe the exact morphology, composition, and size of inclusions. For the related experiment, a 10wt% AA solution (10wt% acetylacetone–1wt% tetramethylammonium chloride–methanol) was used as the electrolyte, and a 300 mA current was applied for 4 h. The solution preparation method has been described elsewhere [47]. A vacuum pump was used to filter out the extracted inclusions, which were laid on a membrane filter with a pore size of 0.1 μm. The film was dried, and the filter was coated with platinum.

Then, inclusions on the filter were evaluated using a field-emission scanning electron microscope (SEM; TESCAN model MIRA 3) equipped with an energy-dispersive X-ray spectroscope (EDS).

3. Results and discussion

3.1. Evolution of steel composition after ESR process

Table 3 lists the chemical compositions of steel samples obtained from various parts of the remelted ingot. Comparison of the compositions of the consumable electrode and remelted ingot (Tables 1 and 3, respectively) revealed that the B contents of steel samples at various locations of the remelted ingot were nearly the same or slightly lower than those in the consumable electrode, which indicates that the designed slag composition (Table 1) is applicable to the ESR of 9CrMoCoB steel. The B content of the ingot was governed by the following reaction [11]:

$$4[\mathrm{B}] + 3(\mathrm{SiO_2}) = 3[\mathrm{Si}] + 2(\mathrm{B_2O_3}),$$

$$\lg K_1 = \lg \frac{a^2_{\mathrm{R,B_2O_3}} \cdot a^3_{\%,\,\mathrm{Si}}}{a^3_{\mathrm{R,SiO_2}} \cdot a^4_{\%,\,\mathrm{B}}} = \frac{5114}{T} + 4.76 \qquad (1)$$

where K_1 is the reaction equilibrium constant; $a_{\%,i}$ refers to the activity of element i in the metal phase, which was referenced to the 1wt% standard state, with mass percentage $[\%i]$ as the concentration unit, and $a_{\mathrm{R},i\mathrm{O}}$ indicates the activity of oxide iO in the slag phase relative to the pure matter as a standard state, with mole fraction X_i as the concentration unit. T represents the absolute temperature (K). From Eq. (1), the B content of the remelted ingot exhibited a close relation to the activities of SiO_2 and B_2O_3 in CaF_2–CaO–Al_2O_3–SiO_2–B_2O_3 slag and temperature. The activities of SiO_2 and B_2O_3 in the slag were calculated by using the ion and molecule coexistence model at 1823 K in the authors' previous study [13]. CaF_2 and B_2O_3 in the ESR-type slag can be evaporated at the operation temperature of the industrial ESR process [48–50], which can possibly alter slag composition, further influence the activities of SiO_2 and B_2O_3, and subsequently result in slight fluctuations of Si and B contents along the height or radius direction of the remelted ingot. In addition, the production of CaO due to the evaporation of CaF_2 can decrease the activity of SiO_2 in slag and increase the Al content of liquid steel. As a result, fresh Al_2O_3 can be precipitated in the remelted ingot, as will be discussed in the following text.

Mitchell and Joshi [51] observed the inhomogeneous temperature distribution of a slag bath and metal pool. Specifically, serious temperature fluctuation of the molten bath occurred at the initial stage of the ESR process [52], which also affected the B content in the remelted ingot. Hou *et al.* [53] conducted the ESR of 1Cr21Ni5Ti stainless steel using a 50 kg ESR furnace. They reported a higher increased rate of FeO (due to iron oxidation) in CaF_2–CaO–Al_2O_3–MgO–SiO_2 slag at the initial stage, which then decreased with remelting time. The slight decrease in B content of the remelted ingot as listed in Table 3 compared with that of the consumable electrode can be ascribed to the abovementioned reasons. The ESR furnace was isolated in a cap, and Ar gas was supplied to the reaction chamber, which resulted in a slight decrease in B content rather than a serious oxidation loss in the remelted ingot.

3.2. Characterization of NMIs in the consumable electrode

Fig. 2 shows the EDS elemental mappings of the typical inclusions, which can be classified as complex oxide and sulfide inclusion surrounded by carbide on the top surface part of the consumable electrode. Fig. 2(a) indicates that the complex oxide inclusion consisted of solid Al_2O_3 and liquid CaO–Al_2O_3–SiO_2–MnO system oxide with a low melting point. The complex inclusion also comprised solid V, Ti, and Cr-containing oxides. Fig. 2(b) indicates that the sulfide inclusion is MnS and the outer carbide layer mainly contains C, W, Fe, and Cr elements. Additionally, pure alumina inclusion can be observed in the consumable electrode as shown in Fig. 2(c). The characterizations of the carbides will be discussed in the following text.

Xuan *et al.* [54] used the sessile drop method to investigate the wettability of liquid iron in contact with the Al_2O_3 substrate at 1815 K. They reported an equilibrium contact angle of 103°. Mukai *et al.* [55] determined the contact angle between liquid Fe–16wt%Cr droplets and Al_2O_3 substrate at 1823 K and observed an equilibrium contact angle of 150°. The results demonstrated the increased contact angle between the metal droplet and alumina substrate after the addition of Cr to liquid iron. Choi and Lee [56] investigated the wetting behavior of solid Al_2O_3 with molten CaO–Al_2O_3–SiO_2 slag at 1873 K and reported that the contact angles ranged from 38° to 75° and increased with the increase in Al_2O_3 content in the slag at a given CaO/SiO_2 ratio. Monaghan *et al.* [57] conducted similar experiments at 1773 K and observed that the contact angle between CaO–Al_2O_3–SiO_2–MgO slag and Al_2O_3 substrate reached 19° to 20°. According to Ohta and Suito, the contact angles between Al_2O_3 and CaO–Al_2O_3 particles

Table 3. Chemical compositions of metal samples at various parts of the remelted ingot wt%

Sample	C	Si	Mn	S	Cr	B	Al	O	Others*	Fe
TS	0.13	0.07	0.08	0.002	10.2	0.003	0.006	0.002	5.7	Bal.
TC	0.15	0.05	0.08	0.002	10.3	0.003	0.006	0.002	5.7	Bal.
BS	0.12	0.05	0.08	0.002	10.2	0.002	0.006	0.002	5.7	Bal.
BC	0.12	0.06	0.08	0.002	10.1	0.003	0.007	0.002	5.7	Bal.

Note: Sample notations TS (BS) and TC (BC) mean that the samples were obtained from the top surface (bottom surface) and top center (bottom center) of the ingot, respectively. *Ni + Mo + V + W + Co.

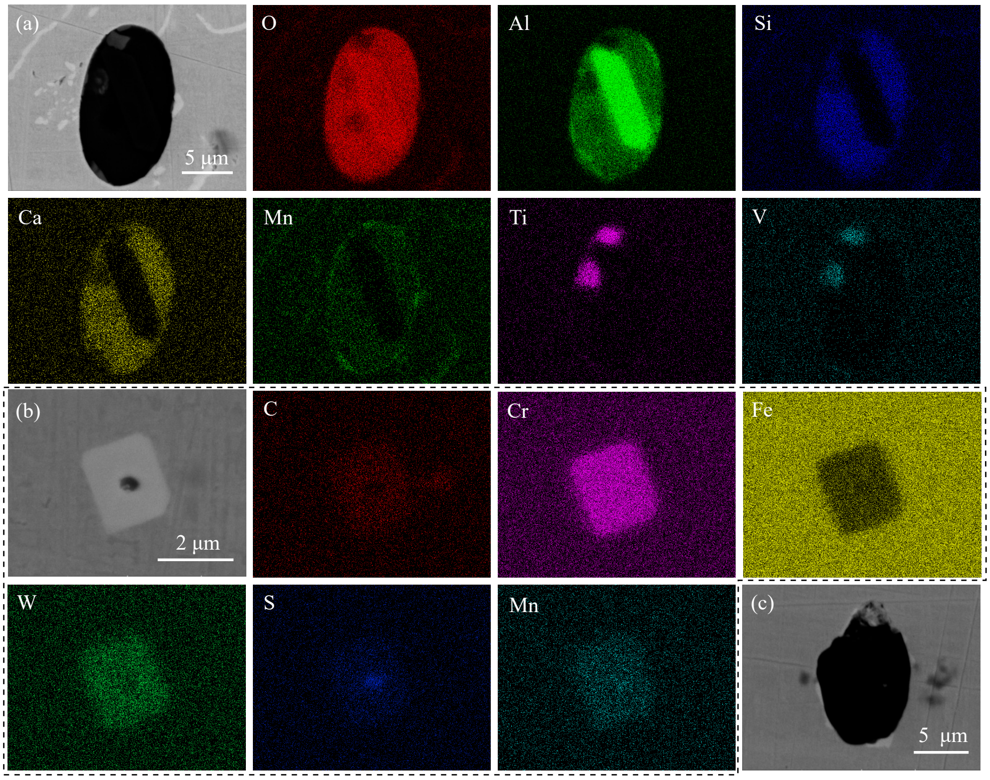

Fig. 2. SEM images and element mappings of typical inclusions observed in the consumable electrode (top surface): (a) complex oxide; (b) MnS surrounded by a carbide layer; (c) Al_2O_3 inclusion.

and liquid iron were 144° and 65°, respectively [58]. Furukawa *et al.* [59] compared the wetting behavior between molten Fe and Fe–18wt%Cr–9wt%Ni alloy NMI-type oxides. The molten Fe had a wetting angle of 114° with an Al_2O_3 substrate, and that of liquid Fe–Cr–Ni alloy was 105° when using the same substrates. Although the wetting angle between molten Fe–Cr–Ni alloy and Al_2O_3 substrate mildly decreased compared with pure liquid iron, both materials remained nonwetted. A similar result was proven by Guo *et al.* [60]. The above results imply that the rectangular Al_2O_3 inclusion that forms during solidification of heat-resistant steel will be pushed into the liquid steel and embedded in liquid $CaO–Al_2O_3–SiO_2–MnO$ inclusion due to the high wetting capability of Al_2O_3 with the $CaO–Al_2O_3–SiO_2–MnO$ system, which may be one of the reasons for the formation of multiphase oxide inclusion as shown in Fig. 2(a). The sulfide–carbide inclusion (Fig. 2(b) is another complex structure containing a MnS core surrounded by an outer carbide layer.

Fig. 3 displays the typical inclusions found at the center of the top part of the consumable electrode and their SEM mapping results, respectively. A comparison of Figs. 2 and 3 revealed the unchanged categories of oxide inclusions. Fig. 3(c) and 3(d) indicate that Al_2O_3-rich oxide and sulfide inclusions can be a core for carbide layer precipitation, respectively. Notably, the MnS inclusion serving as the core of complex inclusion at the center position of the upper electrode shown in Fig. 3(d) is larger than that at the surface due to the higher cooling rate of the surface position than the center part of the upper electrode. The bottom position of the electrode exhibited a similar type of inclusion as shown in Fig. 4. The radius of the MnS inclusion was affected by the sulfur content of liquid steel and the local solidification period, showing an association with the cooling rate [61−62]. Through an *in situ* method, Zeng *et al.* [63] observed the precipitation behavior of MnS in a high-sulfur microalloyed steel at cooling rates of 50 to 400°C/min. In their study, the supersaturation degree of MnS increased, and the local solidification time decreased with the increase in the cooling rate and the number of MnS inclusions; in addition, MnS inclusions became smaller. Xue *et al.* [64] reported the same results. MnS precipitated in the $Al_2O_3–SiO_2$ system inclusion (Fig. 4(a)) due to the low sulfide solubility of the $Al_2O_3–SiO_2$ inclusion, high disregistry between Al_2O_3 and MnS inclusion, or both inclusions, which can act as a nucleation core of carbide. The oxide inclusion mainly comprised Al_2O_3 as confirmed by the elemental mapping results shown in Fig. 4(c). Guo *et al.* [60] observed Al_2O_3, MnS, and $Al_2O_3−MnS$ inclusions in high-speed steel and the 3.75% 2D disregistry between Al_2O_3 $(10\bar{1}4)$ and MnS inclusion (211). Liu *et al.* [65] reported similar results.

3.3. Inclusions in remelted ingot

Characterization of the morphologies and compositions of inclusions in the remelted ingot was conducted to reveal the evolution of inclusions during the ESR of heat-resistant steel. Fig. 5 shows the typical inclusions observed at different positions in the remelted ingot, and Fig. 6 displays elemental mapping results of inclusion as shown in Fig. 5(c). The inclusions consisted of Al_2O_3 alone, and they can act as subsequent nucleation sites for peripheral carbide precipitation.

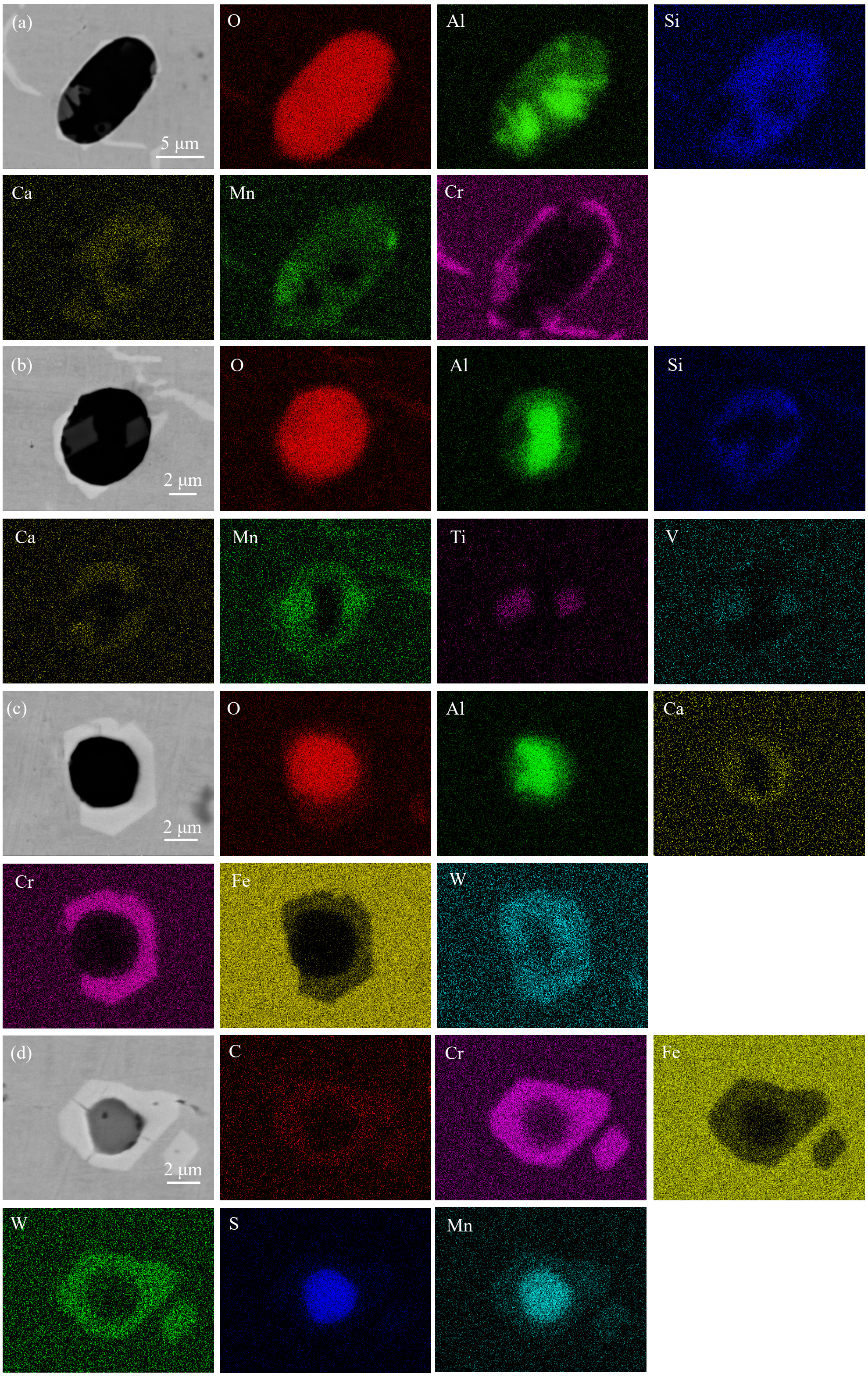

Fig. 3. SEM images and elemental mappings of typical inclusions observed in the consumable electrode (top center): (a–c) Al_2O_3 rich oxide inclusion with carbide layer; (d) MnS surrounded by a carbide layer.

Al_2O_3 inclusions exhibited irregular and angular morphologies. Statistical analysis of inclusion particles in various locations at the electrode and remelted ingot was performed based on the Japanese Industrial Standard (JIS-G-0555). Fig. 7 presents the comparison of the cleanliness of the electrode and remelted ingot before and after the ESR process. As shown in the figure, the ingot attained a considerably higher cleanliness than the consumable electrode at any sampling position. In some cases, the initial inclusions in the electrode remained in the remelted ingot. The sources of large-sized Al_2O_3 inclusions in the remelted ingot (Fig. 5) possibly originated from the electrode or were newly formed. However, no sulfide inclusions were observed in the remelted ingot. The following text will discuss the thermody-

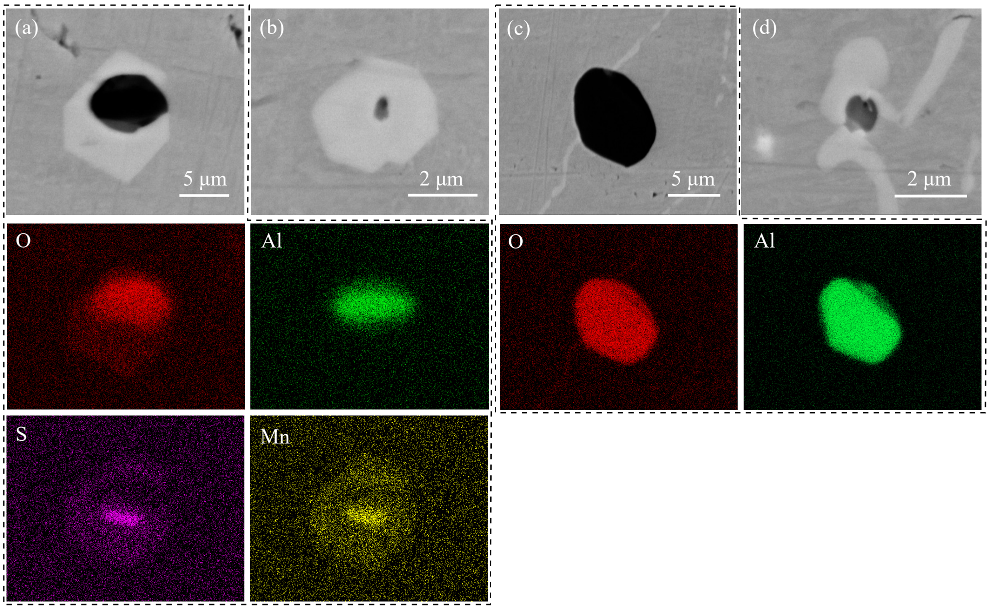

Fig. 4. SEM images and elemental mappings of typical inclusions observed in the consumable electrode at different locations: (a, b) bottom surface and (c, d) bottom center.

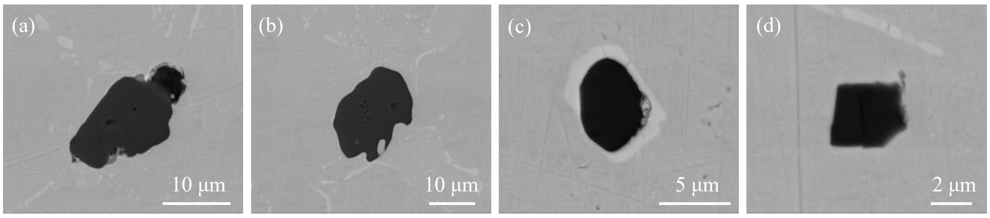

Fig. 5. SEM images of typical inclusions observed in the remelted ingot at various locations: (a) top surface; (b) top center; (c) bottom surface; (d) bottom center.

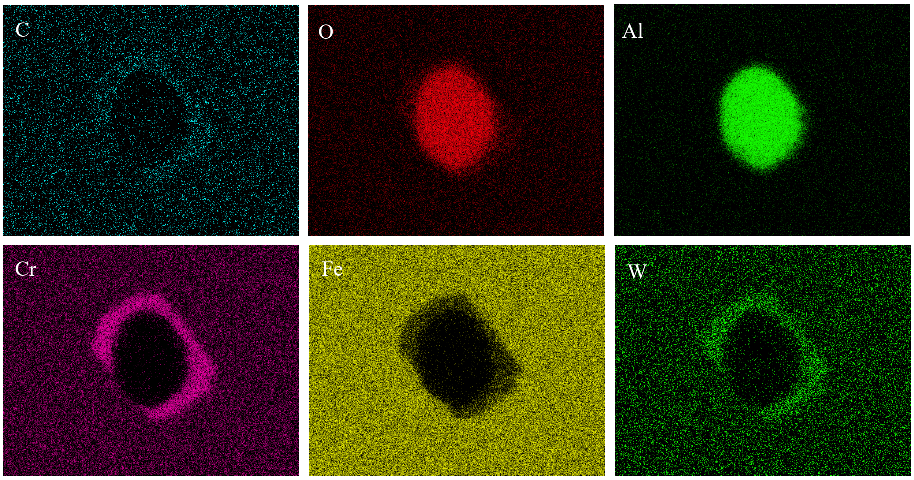

Fig. 6. Elemental maps of the inclusion shown in Fig. 5(c).

namic analysis of the removal and transformation mechanism of inclusions in heat-resistant steel during ESR processing.

3.4. Transformation mechanism of inclusions in the consumable electrode

Multiphase oxide inclusions in the electrode contained CaO (Figs. 2 and 3), which was likely due to the transfer of Ca from slag during the preparation of the consumable electrode in the LF [66]. The determined total Ca content in the steel comprised soluble and insoluble Ca in the inclusions. Free Ca was lower than total calcium and was difficult to measure [67]. A total of 2 ppm Ca was used in calculations for ease of explanation of the formation behavior of inclusions in the consumable electrode. The oxide inclusions contained low amounts of MgO, and thus, the Mg content in steel was neglected in this study.

FactSage™ software (Ver. 8.2, Databases: FToxid and FSstel) was used to calculate the formation and transformation of inclusions in liquid heat-resistant steel with the alloy-

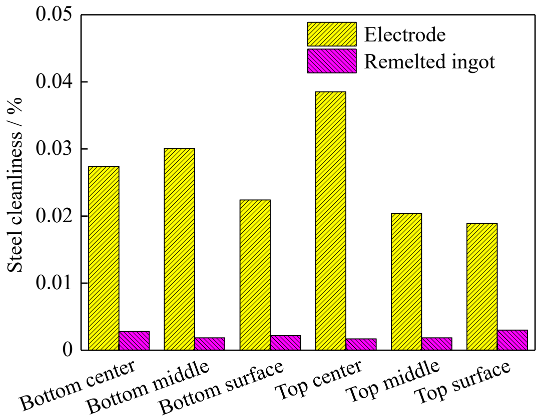

Fig. 7. Cleanliness of the electrode and remelted ingot before and after the ESR process.

ing element Ca (2 ppm) in the consumable electrode as a function of temperature, and the results are illustrated in Fig. 8(a), which shows that liquid oxide inclusions initially formed at 1650°C, followed by calcium aluminate inclusions ($CaAl_2O_7$ and $CaAl_{12}O_{19}$). Fig. 8(b) illustrates the calculated mass fraction of each component in the liquid oxide inclusion. The liquid inclusion mainly consisted of the CaO–Al_2O_3–SiO_2 system containing a small amount of MnO, which is in good agreement with the experimental findings presented in Figs. 2 and 3. Pure Al_2O_3 inclusions started to form when the temperature was dropped to approximately the liquidus temperature of the steel (1550°C), and the amount of Al_2O_3 inclusion increased with the decrease in temperature. Therefore, pure Al_2O_3 inclusions can be observed at various sampling positions at the electrode, such as the top and bottom surface at the electrode.

As discussed above, multiphase inclusion, i.e., a solid Al_2O_3 inclusion surrounded by the liquid CaO–Al_2O_3–SiO_2 system oxide inclusion, was formed due to the higher contact angle of Al_2O_3 particles at the solid/liquid front of steel compared with that of liquid CaO–Al_2O_3–SiO_2 system oxide inclusion. As a consequence, the solid Al_2O_3 inclusions were pushed into liquid steel during the lower solidification process and combined with the CaO–Al_2O_3–SiO_2 system oxide inclusion. On the other hand, the nucleation rate of Al_2O_3 particles was lower than that of the CaO–Al_2O_3–SiO_2 system at a fixed supersaturation ratio (S_o/S_o^*) at 1873 K [68], which indicates the embedment of Al_2O_3 particles in the CaO–Al_2O_3–SiO_2 system inclusion.

FactSage^{TM} 8.2 software was used to calculate the nonequilibrium solidification curve of liquid steel, and the results are presented in Fig. 9. Thermodynamic analysis revealed that liquid inclusion was mainly composed of the CaO–Al_2O_3–SiO_2 system during the equilibrium (Fig. 8(b)) and nonequilibrium cooling processes (Fig. 9(b)). However, the calcium aluminate inclusions ($CaAl_2O_7$ and $CaAl_{12}O_{19}$) in Fig. 8(a) cannot be observed in Fig. 9(a), which proves the

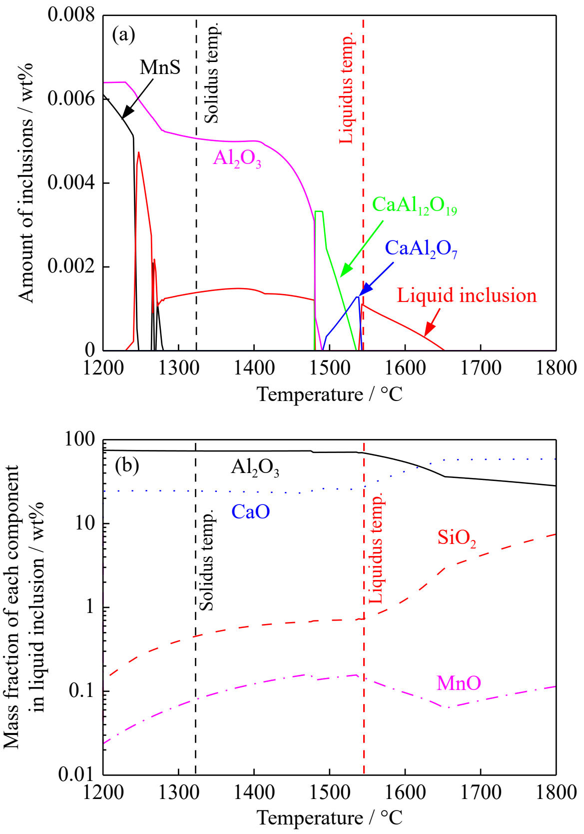

Fig. 8. (a) Equilibrium solidification curves of the electrode and (b) change in mass fraction of each component in the liquid inclusion as a function of temperature calculated using FactSage^{TM} 8.2 software.

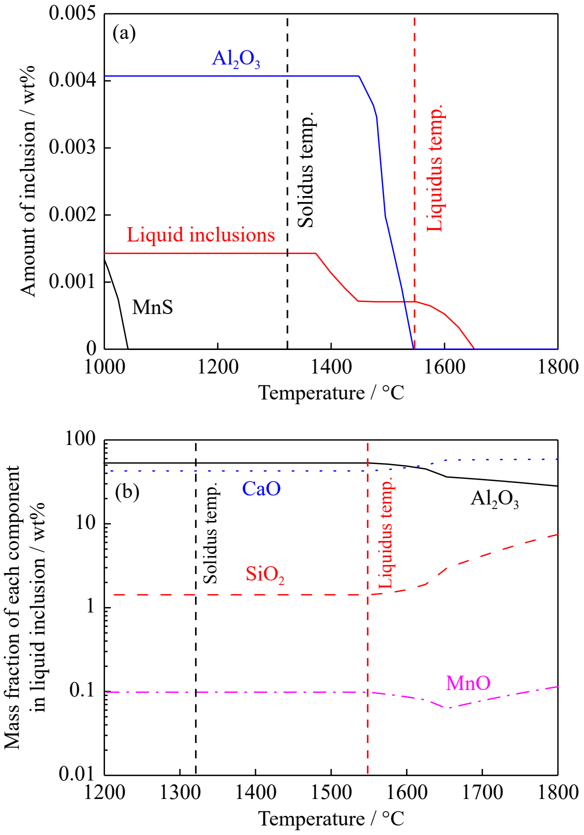

Fig. 9. (a) Scheil solidification curves of the electrode and (b) changes in mass fraction of each component in liquid inclusion as a function of temperature calculated using FactSage^{TM} 8.2 software.

manufacture of a larger heat-resistant consumable electrode during the nonequilibrium cooling process. This finding is in accordance with the experimental results shown in Figs. 2(a), 3(a), and 3(b).

After full solidification of liquid heat-resistant steel, precipitation of MnS inclusions can occur at temperatures lower than 1300°C. To explain the precipitation behavior of MnS and carbide, as displayed in Figs. 2(b) and 3(d), respectively, we also calculated a similar equilibrium solidification curve of liquid heat-resistant steel using Thermo-Calc^{TM} 2022b with a TCFE12 database at the temperature range between 600 and 1600°C (Fig. 10). The calculated precipitation temperatures of MnS inclusion using the abovementioned thermodynamic software (FactSage^{TM} and Thermo-Calc^{TM}) were almost the same, *ca.* 1250°C and 1210°C, during the equilibrium cooling process shown in Figs. 8(a) and 10, respectively. The estimated formation temperature of MnS during the nonequilibrium solidification process (Fig. 9(a), approximately 1050°C) was lower than that during the equilibrium solidification process due to the higher cooling rate under nonequilibrium solidification [69]. It can be observed from the thermodynamic calculation results that the order of precipitation temperature was $M_{23}C_6$ carbides < MnS < Al_2O_3 particles.

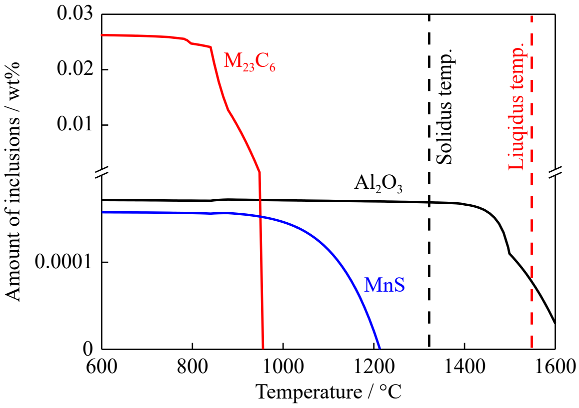

Fig. 10. Equilibrium solidification curves of the electrode calculated using Thermo-Calc^{TM} software.

According to the results, the formerly precipitated MnS and/or Al_2O_3 inclusions acted as heterogeneous nucleation sites for the formation of $M_{23}C_6$-type carbides (Figs. 3(c), 3(d), and 4(a)). After full solidification of steel, the carbide precipitates comprised nanometer-sized secondary carbides [70], which differs from the experimental findings in Figs. 2–5. Therefore, the $M_{23}C_6$ carbides observed via the SEM in this study should have been formed during the solidification process of liquid steel. The accumulation of alloying elements at the solid/liquid front due to microsegregation can thermodynamically benefit carbide formation. Nevertheless, a high cooling rate would result in inadequate time for the growth of carbides at the top surface position of the electrode and ingot. Similar results regarding the precipitation of MnS have been reported in the author's previous study [62]. Fig. 11 displays the 3D morphologies of carbides extracted from the consumable electrode at various locations. The composition and size of carbides were easily identified using the proposed method. The $M_{23}C_6$-type carbide exhibited hexahedron, octahedron, and dodecahedron morphologies.

Fig. 11(j) and (k) show the EDS spectra corresponding to the carbides in Fig. 11(h) and (i) at the bottom surface position of the electrode, respectively. The results indicate that the $M_{23}C_6$-type carbides mainly included C, W, Cr, Fe, and Mo. Yoshizawa *et al.* [71] reported a similar structure of $M_{23}C_6$-type carbide in their study on the effect of W on the coarsening of carbide in heat-resistant steel (9Cr–1W–3Co–0.2V–0.05Nb–0.003B, wt%) during creep at elevated temperatures. They observed that W can replace Cr in the $M_{23}C_6$ lattice to form $[Fe_4(Cr,W)_{19}]C_6$. Xiao *et al.* [72] and Sanhueza *et al.* [73] arrived at the same conclusion and revealed that carbide coarsening can be restrained through the addition of the alloying element boron (B); the discontinuous distribution of small-sized carbide along the grain boundary protected against grain boundary sliding, which improved creep strength at high temperatures [7].

The TEM results were obtained to further confirm the type of carbide in 9CrMoCoB steel (Fig. 12). Analysis of diffraction patterns (Fig. 12(a)) determined the types of carbides whose formulations are listed in Table 4. The crystallographic parameters of carbides containing C, W, Cr, Fe, and Mo were selected from the Inorganic Crystal Structure Database. These results indicate that the substitution of Cr with alloying elements (W, Fe, or/and Mo) in the $Cr_{23}C_6$ lattice can slightly change the latter parameter, which explains the match between the carbides listed in Table 4 and the diffraction pattern shown in Fig. 12(a). In addition, the observation of Al_2O_3 inclusion in the electrode displayed in Fig. 12(b) is consistent with the above experimental and thermodynamical results.

3.5. Removal mechanism of inclusions in steel during the ESR process

According to Fraser and Mitchell [74], the temperature at the electrode tip during a stable ESR process approximates the liquidus temperature of steel, and its superheat was not over 20–30 K. The liquidus and solidus temperatures of heat-resistant steel were estimated using FactSage^{TM} 8.2 software (1550°C and 1320°C, respectively). Therefore, the temperature at the electrode tip ranged from 1570 to 1580°C during the actual ESR process. In combination with the thermodynamic analysis results shown in Fig. 9(a), the liquid-metal film at the electrode tip mainly comprised $CaO–Al_2O_3–SiO_2–MnO$ multiphase inclusions (mainly contains Al_2O_3) and pure Al_2O_3 particles, most of which can be absorbed by the liquid $CaF_2–CaO–Al_2O_3–SiO_2–B_2O_3$ slag by coupling with the decomposed outer-layer carbides [37]. The absorption of the formed Al_2O_3–containing inclusions at the electrode tip by $CaF_2–CaO–Al_2O_3–SiO_2–B_2O_3$ slag depended on the total dissolution time (τ) of oxide inclusions, which is defined as the ratio of slag viscosity and concentration difference between oxide inclusions and slag. The expression can be represented as follows [75]:

$$\tau = \frac{\rho\eta}{\Delta C} \tag{2}$$

where ρ, η, and ΔC refer to the density of oxide inclusion

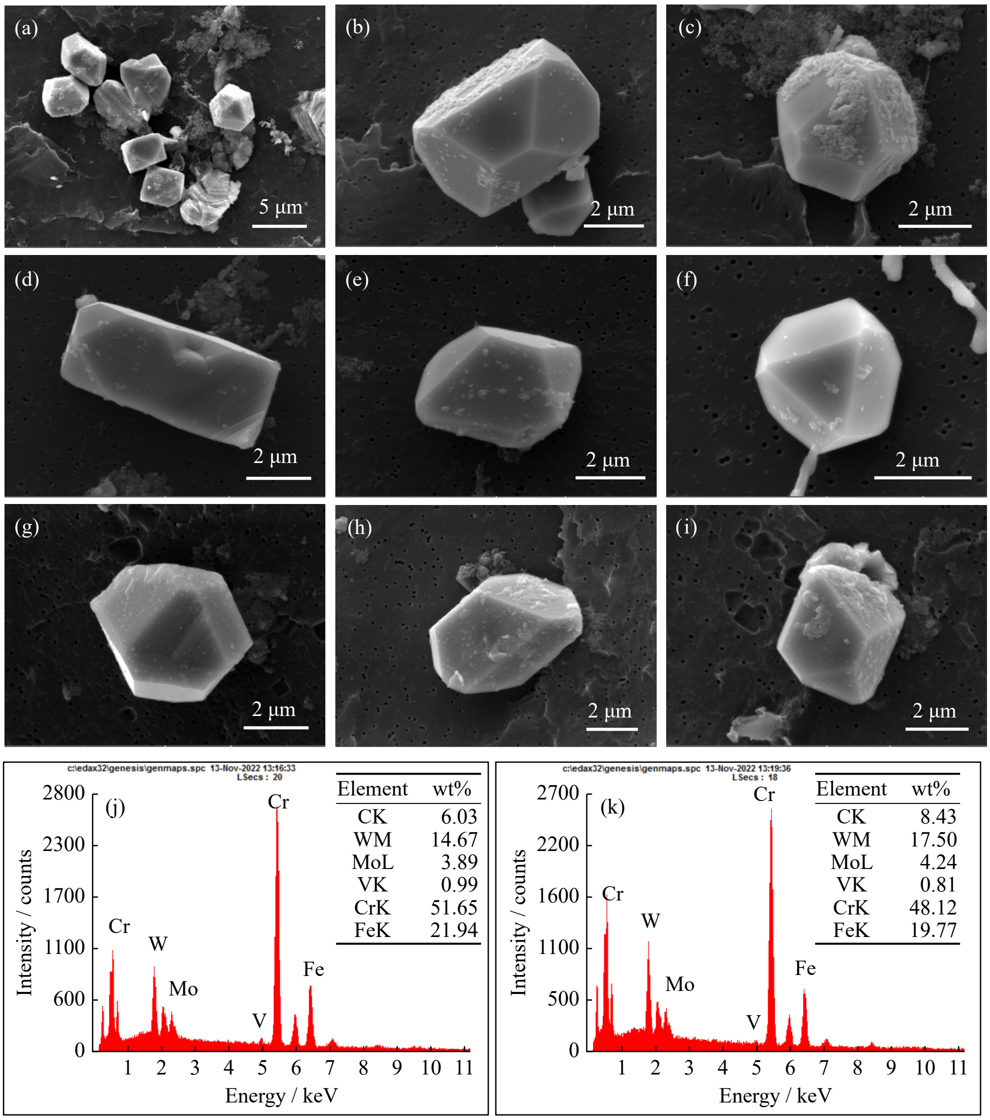

Element	wt%
CK	6.03
WM	14.67
MoL	3.89
VK	0.99
CrK	51.65
FeK	21.94

Element	wt%
CK	8.43
WM	17.50
MoL	4.24
VK	0.81
CrK	48.12
FeK	19.77

Fig. 11. 3D morphologies of electrolytic extraction carbides at various locations in the consumable electrode: (a–c) top center; (d–f) bottom center; (g–i) bottom surface (EDS results shown in (j) and (k) correspond to the carbides displayed in (h) and (i), respectively).

particles, slag viscosity, and driving force of dissolution, respectively. For the Al_2O_3-containing inclusions in the metal film at the electrode, the slag composition with a high CaO content increased the concentration difference $\Delta C\,(Al_2O_3)$ and decreased slag viscosity [76], which benefitted the removal of Al_2O_3-containing inclusions during the ESR process. A similar behavior was reported by Wang *et al.* [45], who observed that a portion of $CaO–Al_2O_3–SiO_2–MnO$ inclusions can be decomposed into their chemical species in liquid steel except for the absorption of quaternary liquid inclusions by the $CaF_2–CaO–Al_2O_3–MgO–SiO_2–B_2O_3$ slag during the ESR process. As mentioned above, some inclusions can remain in the metal droplets that are detached from the electrode tip, pass through the slag bath, and finally accumulate in the liquid-metal pool. Meanwhile, only Al_2O_3 inclusions can be observed in the remelted ingot (Fig. 5).

The precipitation and transformation behavior of inclusions in liquid steel during the nonequilibrium solidification process were estimated using the Scheil–Gulliver model included in FactSage^{TM} 8.2 software under the assumption that solutes were uniformly distributed in the liquid phase, whereas no diffusion of solutes occurred in the solid phase [77]. Fig. 13 displays the calculated result. Only the Al_2O_3 inclusions can be precipitated in the remelted ingot, which is in good agreement with the experimental findings presented in Fig. 5. From an early discussion, $M_{23}C_6$ carbides can be decomposed and dissolved in liquid steel during the ESR process. Nevertheless, they reprecipitated in the remelted ingot, and the formed Al_2O_3 inclusions served as heterogeneous nucleation sites for the $M_{23}C_6$ carbide (Fig. 5(c)).

The precipitation of Al_2O_3 inclusion alone in the remelted ingot can be attributed to the following reasons.

(1) The unremoved liquid multiphase inclusions can be decomposed into individual Ca, Al, Si, Mn, and O and dissolved in liquid steel [78].

(2) The Al content increased from 40 ppm in the electrode to approximately 60 ppm in the remelted ingot despite the slight decrease in the total oxygen content of the remelted in-

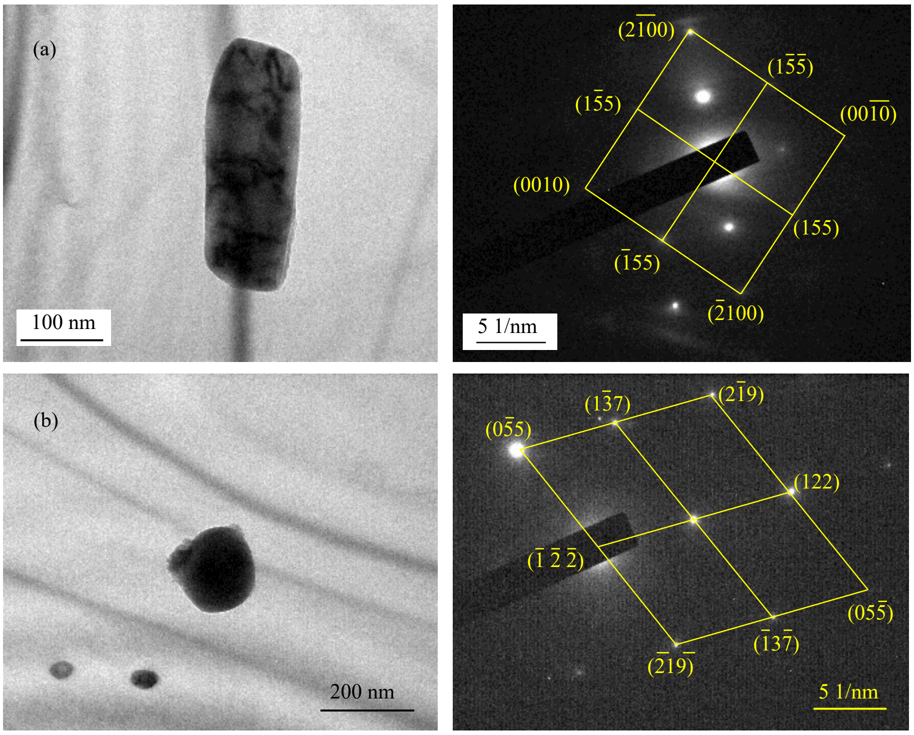

Fig. 12. **TEM images and corresponding diffraction patterns of $Cr_{23}C_6$ carbide (a) and Al_2O_3 inclusion (b) at the top center position of the electrode.**

Table 4. **Crystallographic parameters of $M_{23}C_6$ type carbides**

Phase	Crystal system	Laue class	Lattice parameter / nm
$Cr_{23}C_6$	Cubic	$m\bar{3}m$	1.0767
$Cr_{21.34}Fe_{1.66}C_6$	Cubic	$m\bar{3}m$	1.0645
$(Cr_{19}W_4)C_6$	Cubic	$m\bar{3}m$	1.0790
$Cr_{18.4}Mo_{4.6}C_6$	Cubic	$m\bar{3}m$	1.0900
$Cr_{16}Fe_5Mo_2C_6$	Cubic	$m\bar{3}m$	1.0690

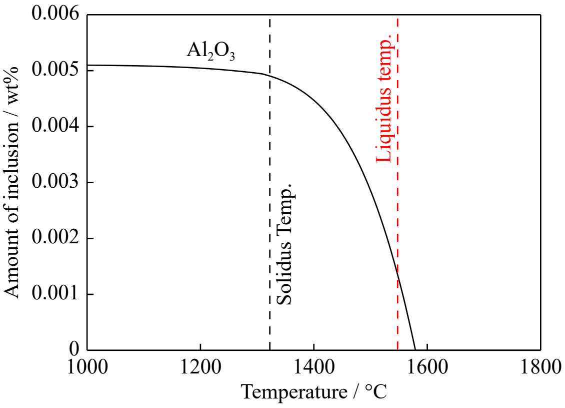

Fig. 13. **Nonequilibrium solidification curve of the remelted ingot calculated using FactSage™ software.**

got. The [Al]–[O] equilibrium in liquid steel [79] and the supersaturation degree of Al_2O_3 [80–81], $S_{Al_2O_3}$, can be calculated through insertion of the equilibrium constant $K^{\ominus}_{Al_2O_3}$ of the reaction in Eq. (4) at 1823 K while considering the precipitation temperature of Al_2O_3 inclusions in the electrode and remelted ingot within 1773 to 1873 K (Figs. 8(a) and 13). The interaction parameters listed in Table 5 [82–83] were employed to calculate the Henrian activity coefficient of Al and O:

$$2[\text{Al}]+3[\text{O}]=(\text{Al}_2\text{O}_3),\Delta G_3^{\ominus}=-1202000+386.3T\ (\text{J/mol}) \tag{3}$$

$$S_{Al_2O_3}=\frac{\left(a^2_{\%,Al}\cdot a^3_{\%,O}\right)}{\left(a^2_{\%,Al}\cdot a^3_{\%,O}\right)_{eq}}=\frac{\left(f^2_{\%,Al}\cdot[\%\text{Al}]^2\cdot f^3_{\%,O}\cdot[\%\text{O}]^3\right)}{\dfrac{1}{K^{\ominus}_{Al_2O_3}}} \tag{4}$$

The calculated supersaturation degree for Al_2O_3 precipitation in the electrode, $S^{\text{Electrode}}_{Al_2O_3}$ and the remelted ingot, $S^{\text{Ingot}}_{Al_2O_3}$ were 1.66 and 1.93 at 1823 K, respectively. Thus, new Al_2O_3 inclusions precipitated in the remelted ingot besides the inherited Al_2O_3 inclusions from the consumable electrode. In the work of Li and Suito [80], the critical supersaturation degrees for Al_2O_3 precipitation in Fe–Al–O and Fe–Al–O–M (M = C, Si, Mn, Ti, Cr) systems reached $\lg S^{\text{Fe–Al–O}}_{Al_2O_3}=3.5$ and $\lg S^{\text{Fe–Al–O–M}}_{Al_2O_3}=0.8$ to 1.3 at 1873 K, which are significantly higher than that obtained in this study. The rationale behind these results may be the high amounts of alloying elements in 9CrMoCoB steel in the present work.

(3) The components of CaO, SiO_2, and MnO in the liquid multiphase inclusions were reduced by the increased Al content in molten steel during the ESR process [84]. The same trend was reported by Wen *et al.* [85] in a study on nonmetallic inclusion evolution during the ESR of Q235B steel. They observed that the increase in Al content in steel transferred from CaF_2–CaO–Al_2O_3–MgO slag resulted in the generation of Al_2O_3 inclusion through reduction reactions between the SiO_2–MnO inclusion and the dissolved Al in molten steel. Our previous publication [14] indicated that the

Table 5. First-order activity coefficients (e_i^j) used in this study [82]

Element i	Element j						
	C	Si	Mn	S	Ni	Cr	Mo
Mn	$-1370/T + 0.69$	$-1838/T + 0.964$	0	−0.048	−0.0072	0.0039	0.0046
S	0.111	0.075	−0.026	$-120/T + 0.018$	0	$-94.2/T + 0.04$	0.0027
Al	0.091	0.056	—	0.035	−0.0173	0.012*	—
O	−0.421	−0.066	−0.021	−0.133	0.006	$-380/T + 0.151$	0.005

Element i	Element j						
	V	Al	Co	W	B	N	O
Mn	0.0057	0	−0.0036	$236/T - 0.12$	−0.0236	−0.091	−0.083
S	−0.019	0.041	0.0026	0.011	0.134	0.01	−0.27
Al	—	$80.5/T$	—	—	—	0.015	−1.98
O	$-1050/T + 0.42$	−1.17	0.008	0.0085	−0.31	−0.14	$-1750/T + 0.76$

Note: *This data is from Ref. [83].

Al content in molten 9CrMoCoB steel was mainly governed by SiO_2 in the CaF_2–CaO–Al_2O_3–SiO_2–B_2O_3 slag, as shown by the reaction given in Eq. (5):

$$4[\mathrm{Al}] + 3(\mathrm{SiO_2}) = 2(\mathrm{Al_2O_3}) + 3[\mathrm{Si}],$$
$$\Delta G_5^\ominus = -720680 + 133T\ (\mathrm{J/mol}) \tag{5}$$

$$\lg K_5^\ominus + \lg\frac{f_{\%,\mathrm{Al}}^4}{f_{\%,\mathrm{Si}}^3} + \lg\frac{[\%\mathrm{Al}]^4}{[\%\mathrm{Si}]^3} = \lg\frac{\gamma_{\mathrm{R,Al_2O_3}}^2}{\gamma_{\mathrm{R,SiO_2}}^3} + \lg\frac{X_{\mathrm{Al_2O_3}}^2}{X_{\mathrm{SiO_2}}^3} \tag{6}$$

where $f_{\%,i}$, $\gamma_{\mathrm{R},i\mathrm{O}}$, and $K_i^\ominus$ refer to the activity coefficient of element i in the metal phase referenced to the 1wt% standard state, activity coefficient of oxide iO in slag phase relative to the pure matter as a standard state, and the standard equilibrium constant, respectively.

Given the high volatilization potential of CaF_2 in ESR-type slags at high temperatures [48,86–87], the product (CaO) can cause a decrease in SiO_2 activity in liquid slag, which further increased the Al content and decreased that of Si in the remelted ingot compared with that in the electrode. Fig. 14 shows the relationship between the CaO content of CaF_2–CaO–Al_2O_3–SiO_2–B_2O_3 slag and the calculated $\lg(a_{\mathrm{R,Al_2O_3}}^2/a_{\mathrm{R,SiO_2}}^2)$ at 1823 K. The activities of Al_2O_3 and SiO_2 were calculated using the ion and molecule coexistence theory, with the calculation process given in Ref. [14]. Fig. 14 shows that the calculated $\lg(a_{\mathrm{R,Al_2O_3}}^2/a_{\mathrm{R,SiO_2}}^2)$ increased with the increase in CaO content in the slag, which indicates the possible increase in Al content in liquid steel.

Eqs. (7) and (8) express the standard and actual Gibbs free energy of MnS formation reaction in liquid steel, respectively [63]:

$$[\mathrm{Mn}] + [\mathrm{S}] = (\mathrm{MnS}), \Delta G_7^\ominus = -177600 + 99.5T\ (\mathrm{J/mol}) \tag{7}$$

$$\Delta G_7 = \Delta G_7^\ominus + RT\ln\frac{a_{\mathrm{R,MnS}}}{f_{\%,\mathrm{Mn}}\cdot[\%\mathrm{Mn}]\cdot f_{\%,\mathrm{S}}\cdot[\%\mathrm{S}]} \tag{8}$$

where the activity coefficients $f_{\%,\mathrm{Mn}}$ and $f_{\%,\mathrm{S}}$ can be calculated utilizing the Wagner formulation [88] and relative interaction parameters listed in Table 5, respectively. Substitution of the activity coefficient values into Eq. (8) resulted in the following expression:

$$\Delta G_7 = -177600 + 98.5T + RT\ln([\%\mathrm{Mn}]\cdot[\%\mathrm{S}]) \tag{9}$$

Scheil formulation can be used to calculate the changes in Mn and S contents in the residual liquid phase as a function of solidification fraction f_s during the solidification process [89]:

$$C_{\mathrm{L},i} = C_{0,i}(1 - f_s)^{(k_i - 1)} \tag{10}$$

where $C_{\mathrm{L},i}$ and $C_{0,i}$ refer to the concentration of component i in molten steel in the solidification process and the initial concentration, respectively, and k_i denotes the equilibrium

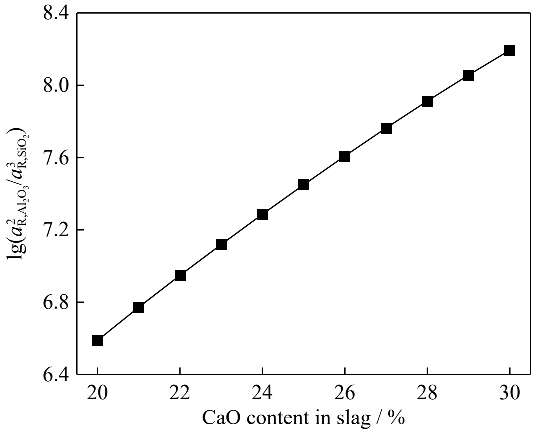

Fig. 14. Relationship between the CaO content in CaF_2–CaO–Al_2O_3–SiO_2–B_2O_3 slag and the calculated $\lg(a_{\mathrm{R,Al_2O_3}}^2)/(a_{\mathrm{R,SiO_2}}^2)$ at 1823 K.

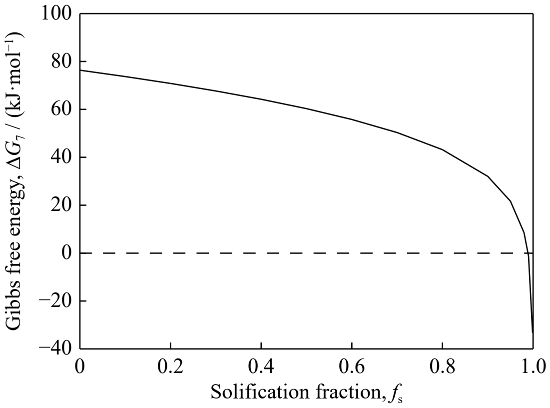

Fig. 15. Relationship between Gibbs free energy of MnS formation and solidification fraction f_s.

partition coefficient of component i. k_{Mn} and k_{S} are 0.035 and 0.785, respectively [90]. Eq. (11) was deduced through insertion of Eq. (10) into Eq. (9):

$$\Delta G_7 = -177600 + 98.5T - RT\ln\left([\%\mathrm{Mn}]_0 \cdot [\%\mathrm{S}]_0 \cdot (1 - f_s)^{-1.18}\right) \tag{11}$$

Fig. 15 shows the relationship between the Gibbs free energy of MnS precipitation and solidification fraction f_s. The Gibbs free energy of MnS precipitation decreased with the increase in f_s and tended to be negative when f_s approached 1.0, which implies that MnS can only be formed in solid steel as a result of the microsegregation of Mn and S at the solid/liquid interface.

By contrast, the MnS inclusions can be decomposed into soluble Mn and S in liquid steel, as shown by the backward reaction in Eq. (7), when the temperature rose above the liquidus temperature of steel. Based on the desulfurization reaction in Eq. (12), the dissolved S in liquid steel can be further transferred to the slag by combining with CaO in the CaF_2–CaO–Al_2O_3–SiO_2–B_2O_3 ESR-type slag.

$$[\mathrm{S}] + (\mathrm{O}^{2-}) = (\mathrm{S}^{2-}) + [\mathrm{O}] \tag{12}$$

Hou *et al.* [91] reported the high desulfurization efficiency of ESR operation, with the rate-controlling step of desulfurization reaction involving the mass transfer of sulfur in the liquid-metal phase. Wang *et al.* [92] restudied the effect of B_2O_3 on the physicochemical properties of $7CaF_2$–$50CaO$–$20Al_2O_3$–$8MgO$–$15SiO_2$–B_2O_3 (wt%) slag and observed decreased melting point and viscosity; moreover, the desulfurization capability increased after the addition of 4wt% B_2O_3 to the slag. In this study, the sulfur content of ingot was approximately 20 ppm, and the calculated activity coefficients of Mn and S and the precipitation temperature of MnS (1323 K) were incorporated in Eq. (9). The results indicate that $\Delta G_7 > 0$, and the amount of sulfur was extremely low to form sulfide inclusions in the remelted ingot. Wang *et al.* reported a similar behavior [45].

MnS inclusions were wrapped by a $M_{23}C_6$ carbide shell (Figs. 2(b), 3(d), 4(b), and 4(d)), which precipitated at approximately 950°C. Thus, the dissociation reaction of MnS inclusion involved the coupling with $M_{23}C_6$ carbide decomposition at the electrode tip. Zhu *et al.* [93] observed the decreased total area and average size of $M_{23}C_6$ and M_7C_3 carbides in 8Cr13MoV martensitic stainless steel after the ESR process; they suggested that ESR can facilitate the reduction of primary carbide in the electrode. This finding explains the lack of MnS inclusions in the remelted ingot.

4. Conclusions

Industrial experiments were conducted in an 80-t ESR furnace under an Ar gas atmosphere to manufacture a large 9Cr-MoCoB heat-resistant steel ingot. A systematic investigation was conducted on the evolutionary behavior of nonmetallic inclusions at various locations (top center, top surface, bottom center, and bottom surface) in the electrode and remelted ingot. Thermodynamic analysis was focused on the formation and removal behavior of inclusions in steel during the ESR process. The main conclusions can be summarized as follows.

(1) The main types of oxide inclusions in the electrode comprised pure Al_2O_3 and a liquid multiphase CaO–Al_2O_3–SiO_2–MnO inclusion with an Al_2O_3 island. The formation of multiphase inclusions was likely due to the higher contact angle between the Al_2O_3 inclusion and liquid steel than that between Al_2O_3 inclusion and the liquid CaO–Al_2O_3 higher SiO_2 higher MnO system inclusion.

(2) The $M_{23}C_6$-type carbide that formed in heat-resistant steel mainly contained C, Fe, Cr, Mo, and W. The order of precipitation temperatures was as follows: Al_2O_3 > MnS > $M_{23}C_6$-type carbide. Hence, Al_2O_3 and MnS can act as nucleation sites for the precipitation of $M_{23}C_6$-type carbide. The $M_{23}C_6$-type carbides were determined as $Cr_{23}C_6$, $Cr_{23}C_6$ carbide, $Cr_{21.34}Fe_{1.66}C_6$, $(Cr_{19}W_4)C_6$, $Cr_{18.4}Mo_{4.6}C_6$, or $Cr_{16}Fe_5Mo_2C_6$ after the analysis of TEM results.

(3) The removal of the liquid multiphase CaO–Al_2O_3–SiO_2–MnO inclusion occurred due to absorption by the liquid CaF_2–CaO–Al_2O_3–SiO_2–B_2O_3 slag, decomposition, further dissolution into the liquid steel, and reduction of CaO, SiO_2, and MnO by the increased Al content in liquid steel during the ESR process. The MnS inclusions in the consumable electrode were decomposed and dissolved in liquid steel, and the sulfur content dropped to 20 ppm, which is extremely low to form the sulfide inclusion in the remelted ingot due to the high desulfurization efficiency of the ESR process.

(4) The remelted ingot comprised pure Al_2O_3 and Al_2O_3-core inclusions surrounded by a carbide shell. The new Al_2O_3 inclusions formed when the supersaturation degree of Al_2O_3 precipitation in the electrode $S_{\mathrm{Al_2O_3}}^{\mathrm{Electrode}}$ became lower than that in the remelted ingot $S_{\mathrm{Al_2O_3}}^{\mathrm{Electrode}}$ except for that inherited from the electrode. The evaporation of CaF_2 resulted in the increased CaO content of the ESR-type slag and further increased in the Al content in liquid steel during the ESR process. Consequently, the increased Al content in liquid steel either generated a new Al_2O_3 inclusion or reduced the components (CaO, SiO_2, and MnO) of the liquid CaO–Al_2O_3–SiO_2–MnO inclusion to form Al_2O_3 inclusion in the remelted ingot.

Acknowledgements

This work was partly supported by the Korea Evaluation Institute of Industrial Technology (KEIT, No. 20009956) and by the Korea Institute for Advancement of Technology (KIAT, No. P0023676, HRD Program for Industrial Innovation), funded by the Ministry of Trade, Industry and Energy (MOTIE), Korea. W.Z. Mu would like to acknowledge the Swedish Foundation for International Cooperation in Research and Higher Education (STINT) for supporting the collaboration between KTH (Sweden) and Hanyang University (Korea). S.C. Duan would like to acknowledge G.H. Yang and J. Kim at Hanyang University for their help with TEM measurements.

Conflict of Interest

Wangzhong Mu and Joo Hyun Park are editorial board members for this journal and were not involved in the editorial review or the decision to publish this article. There are no conflicts of interest to declare.

References

[1] T. Horiuchi, M. Igarashi, and F. Abe, Improved utilization of added B in 9Cr heat-resistant steels containing W, *ISIJ Int.*, 42(2002), p. S67.

[2] F. Masuyama, History of power plants and progress in heat resistant steels, *ISIJ Int.*, 41(2001), No. 6, p. 612.

[3] W. Yan, W. Wang, Y.Y. Shan, K. Yang, and W. Sha, *9-12Cr Heat-Resistant Steels*, Springer International Publishing, Cham, 2015.

[4] F. Abe, Precipitate design for creep strengthening of 9% Cr tempered martensitic steel for ultra-supercritical power plants, *Sci. Technol. Adv. Mater.*, 9(2008), No. 1, art. No. 013002.

[5] X.B. Hu, L. Li, X.C. Wu, and M. Zhang, Coarsening behavior of M23C6 carbides after ageing or thermal fatigue in AISI H13 steel with niobium, *Int. J. Fatigue*, 28(2006), No. 3, p. 175.

[6] X.S. Zhou, C.X. Liu, L.M. Yu, Y.C. Liu, and H.J. Li, Phase transformation behavior and microstructural control of high-Cr martensitic/ferritic heat-resistant steels for power and nuclear plants: A review, *J. Mater. Sci. Technol.*, 31(2015), No. 3, p. 235.

[7] Y.H. Zhou, Y.C. Liu, X.S. Zhou, *et al*., Precipitation and hot deformation behavior of austenitic heat-resistant steels: A review, *J. Mater. Sci. Technol.*, 33(2017), No. 12, p. 1448.

[8] R.L. Klueh, Elevated temperature ferritic and martensitic steels and their application to future nuclear reactors, *Int. Mater. Rev.*, 50(2005), No. 5, p. 287.

[9] Z. Liu, X.T. Wang, and C. Dong, Effect of boron on G115 martensitic heat resistant steel during aging at 650°C, *Mater. Sci. Eng. A*, 787(2020), art. No. 139529.

[10] M. Sharma, I. Ortlepp, and W. Bleck, Boron in heat-treatable steels: A review, *Steel Res. Int.*, 90(2019), No. 11, art. No. 1900133.

[11] D.S. Kim, G.J. Lee, M.B. Lee, J.I. Hur, and J.W. Lee, Manufacturing of 9CrMoCoB steel of large ingot with homogeneity by ESR process, *IOP Conf. Ser. Mater. Sci. Eng.*, 143(2016), art. No. 012002.

[12] L.Z. Peng, Z.H. Jiang, and X. Geng, Design of ESR slag for remelting 9CrMoCoB steel through experiments and thermodynamic calculations, *Calphad*, 70(2020), art. No. 101782.

[13] S.C. Duan and J.H. Park, Comparison of oxidation behavior of various reactive elements in alloys during electroslag remelting (ESR) process: An overview, *ISIJ Int.*, 62(2022), No. 8, p. 1561.

[14] S.C. Duan, M.J. Lee, D.S. Kim, and J.H. Park, Oxidation behavior of boron in 9CrMoCoB steel by CaF_2–CaO–Al_2O_3–SiO_2–B_2O_3 electroslag remelting (ESR) type slag, *J. Mater. Res. Technol.*, 17(2022), p. 574.

[15] J.H. Park and Y. Kang, Inclusions in stainless steels–A review, *Steel Res. Int.*, 88(2017), No. 12, art. No. 1700130.

[16] J.H. Park and H. Todoroki, Control of MgO·Al_2O_3 spinel inclusions in stainless steels, *ISIJ Int.*, 50(2010), No. 10, p. 1333.

[17] J.H. Park and L.F. Zhang, Kinetic modeling of nonmetallic inclusions behavior in molten steel: A review, *Metall. Mater. Trans. B*, 51(2020), No. 6, p. 2453.

[18] S.F. Yang, S.L. Yang, J.L. Qu, *et al*., Inclusions in wrought superalloys: A review, *J. Iron Steel Res. Int.*, 28(2021), No. 8, p. 921.

[19] K.O. Findley, J.L. Evans, and A. Saxena, A critical assessment of fatigue crack nucleation and growth models for Ni- and Ni, Fe-based superalloys, *Int. Mater. Rev.*, 56(2011), No. 1, p. 49.

[20] R.T. Holt and W. Wallace, Impurities and trace elements in nickel-base superalloys, *Int. Met. Rev.*, 21(1976), No. 1, p. 1.

[21] X.Y. Gao, L. Zhang, X.H. Qu, X.W. Chen, and Y.F. Luan, Effect of interaction of refractories with Ni-based superalloy on inclusions during vacuum induction melting, *Int. J. Miner. Metall. Mater.*, 27(2020), No. 11, p. 1551.

[22] J. Wang, L.Z. Wang, J.Q. Li, C.Y. Chen, S.F. Yang, and X. Li, Effects of aluminum and titanium additions on the formation of nonmetallic inclusions in nickel-based superalloys, *J. Alloys Compd.*, 906(2022), art. No. 164281.

[23] A.J. Shi, Z. Wang, C.B. Shi, L. Guo, C.Q. Guo, and Z.C. Guo, Supergravity-induced separation of oxide and nitride inclusions from inconel 718 superalloy melt, *ISIJ Int.*, 60(2020), No. 2, p. 205.

[24] K.A. Al-Jarba and G.E. Fuchs, Effect of carbon additions on the as-cast microstructure and defect formation of a single crystal Ni-based superalloy, *Mater. Sci. Eng. A*, 373(2004), No. 1-2, p. 255.

[25] L.Z. He, Q. Zheng, X.F. Sun, *et al*., Effect of carbides on the creep properties of a Ni-base superalloy M963, *Mater. Sci. Eng. A*, 397(2005), No. 1-2, p. 297.

[26] L.R. Liu, T. Jin, N.R. Zhao, X.F. Sun, H.R. Guan, and Z.Q. Hu, Formation of carbides and their effects on stress rupture of a Ni-base single crystal superalloy, *Mater. Sci. Eng. A*, 361(2003), No. 1-2, p. 191.

[27] S.L. Yang, S.F. Yang, W. Liu, J.S. Li, J.G. Gao, and Y. Wang, Microstructure, segregation and precipitate evolution in directionally solidified GH4742 superalloy, *Int. J. Miner. Metall. Mater.*, 30(2023), No. 5, p. 939.

[28] V.T. Ha and W.S. Jung, Niobium carbo-nitride precipitation behavior in a high nitrogen 15Cr-15Ni heat resistant austenitic stainless steel, *Met. Mater. Int.*, 17(2011), No. 5, p. 713.

[29] W.R. Sun, S.R. Guo, D.Z. Lu, and Z.Q. Hu, Effect of sulfur on the solidification and segregation in Inconel 718 alloy, *Mater. Lett.*, 31(1997), No. 3-6, p. 195.

[30] E.P. Whelan and M.S. Grzedzielski, H-phase sulphocarbides and sulphur in nickel-base superalloys, *Met. Technol.*, 1(1974), No. 1, p. 186.

[31] X.C. Chen, C.B. Shi, H.J. Guo, F. Wang, H. Ren, and D. Feng, Investigation of oxide inclusions and primary carbonitrides in inconel 718 superalloy refined through electroslag remelting process, *Metall. Mater. Trans. B*, 43(2012), No. 6, p. 1596.

[32] X. Shi, S.C. Duan, W.S. Yang, M.T. Mao, H.J. Guo, and J. Guo, Effects of remelting current on structure, composition, microsegregation, and inclusions in inconel 718 electroslag remelting ingots, *Metall. Mater. Trans. B*, 50(2019), No. 6, p. 3072.

[33] S.C. Duan, X. Shi, F. Wang, *et al*., Investigation of desulfurization of Inconel 718 superalloys by ESR type slags with different TiO_2 content, *J. Mater. Res. Technol.*, 8(2019), No. 3, p. 2508.

[34] K. Sakuraya, H. Okada, and F. Abe, BN type inclusions formed in high Cr ferritic heat resistant steel, *Energy Mater.*, 1(2006), No. 3, p. 158.

[35] Y. Li, C. Liu, T. Zhang, M. Jiang, and C. Peng, Inclusions modification in heat resistant steel containing rare earth elements, *Ironmaking Steelmaking*, 45(2018), No. 1, p. 76.

[36] L. Zhang, Y.H. Hou, Y.C. Li, Z.L. Xiang, and E.G. Wang, Size and type of inclusions in Fe–Cr–Co Heat–resistant steel and elevated-temperature strength under the effect of electromagnetic stirring, *ISIJ Int.*, 59(2019), No. 6, p. 1049.

[37] Z.B. Li, *Electroslag Metallurgy Theory and Practice*, Metallurgical Industry Press, Beijing, 2010, p. 66.

[38] Z.H. Jiang, *Electroslag Metallurgy*, Science Press, Beijing, 2015.

[39] A. Kharicha, E. Karimi-Sibaki, M.H. Wu, A. Ludwig, and J.

Bohacek, Review on modeling and simulation of electroslag remelting, *Steel Res. Int.*, 89(2018), No. 1, art. No. 1700100.

[40] J. Fu and J. Zhu, Changes in oxide inclusions during electroslag remelting, *Acta Metall. Sin.*, 7(1964), No. 3, p. 250.

[41] A. Mitchell and M. Bell, On the origin of oxide inclusions in ingots made by the electroslag process, *Can. Metall. Q.*, 11(1972), No. 2, p. 363.

[42] Y.W. Dong, Z.H. Jiang, Y.L. Cao, A. Yu, and D. Hou, Effect of slag on inclusions during electroslag remelting process of die steel, *Metall. Mater. Trans. B*, 45(2014), No. 4, p. 1315.

[43] Q. Wang, R.T. Wang, Z. He, G.Q. Li, B.K. Li, and H.B. Li, Numerical analysis of inclusion motion behavior in electroslag remelting process, *Int. J. Heat Mass Transf.*, 125(2018), p. 1333.

[44] X.C. Huang, B.K. Li, Z.Q. Liu, M.Z. Li, and F.S. Qi, Modeling of fluid flow, heat transfer and inclusion removal in electroslag remelting process with a rotating electrode, *Int. J. Heat Mass Transf.*, 163(2020), art. No. 120473.

[45] S.J. Wang, C.B. Shi, Y.J. Liang, X.X. Wan, and X. Zhu, Evolution and formation of Non-metallic inclusions during electroslag remelting of a heat-resistant steel for ultra-supercritical power plants, *Metall. Mater. Trans. B*, 53(2022), No. 5, p. 3095.

[46] Y. Zhao, C.B. Shi, S.J. Wang, P. Ren, and J. Li, Reoxidation of liquid steel and evolution of inclusions during protective atmosphere electroslag remelting of Ce-containing heat-resistant stainless steel, *J. Iron Steel Res. Int.*, (2023). DOI: 10.1007/s42243-023-01092-3

[47] J.H. Park, D.J. Kim, and D.J. Min, Characterization of nonmetallic inclusions in high-manganese and aluminum-alloyed austenitic steels, *Metall. Mater. Trans. A*, 43(2012), No. 7, p. 2316.

[48] J.H. Park and D.J. Min, Thermodynamics of fluoride vaporisation from slags containing CaF_2 at 1773 K, *Steel Res. Int.*, 75(2004), No. 12, p. 807.

[49] Y. Liu, Y. Wang, G.Q. Li, C. Yuan, R. Lu, and B.K. Li, Investigation on the structure, fluoride vaporization and crystallization behavior of CaF_2–CaO–Al_2O_3–(SiO_2) slag for electroslag remelting, *J. Therm. Anal. Calorim.*, 139(2020), No. 2, p. 923.

[50] C.H. Dai, X.P. Zhang, and L. Shui, A new method for measuring activities in slags containing a volatile component, *Metall. Mater. Trans. B*, 26(1995), No. 3, p. 651.

[51] A. Mitchell and S. Joshi, The thermal characteristics of the electroslag process, *Metall. Trans.*, 4(1973), No. 3, p. 631.

[52] R. Schneider, V. Wiesinger, S. Gelder, A. Mitchell, and D. David, Effect of different remelting parameters on slag temperature and energy consumption during ESR, *ISIJ Int.*, 62(2022), No. 6, p. 1199.

[53] D. Hou, Z.H. Jiang, Y.W. Dong, W. Gong, Y.L. Cao, and H.B. Cao, Effect of slag composition on the oxidation kinetics of alloying elements during electroslag remelting of stainless steel: Part-2 control of titanium and aluminum content, *ISIJ Int.*, 57(2017), No. 8, p. 1410.

[54] C. Xuan, H. Shibata, S. Sukenaga, P.G. Jönsson, and K. Nakajima, Wettability of Al_2O_3, MgO and Ti_2O_3 by liquid iron and steel, *ISIJ Int.*, 55(2015), No. 9, p. 1882.

[55] K. Mukai, Z.S. Li, and M. Zeze, Surface tension and wettability of liquid Fe–16 mass%Cr–O alloy with alumina, *Mater. Trans.*, 43(2002), No. 7, p. 1724.

[56] J.Y. Choi and H.G. Lee, Wetting of solid Al_2O_3 with molten CaO-Al_2O_3-SiO_2, *ISIJ Int.*, 43(2003), No. 9, p. 1348.

[57] B.J. Monaghan, H. Abdeyazdan, N. Dogan, M.A. Rhamdhani, R.J. Longbottom, and M.W. Chapman, Effect of slag composition on wettability of oxide inclusions, *ISIJ Int.*, 55(2015), No. 9, p. 1834.

[58] H. Ohta and H. Suito, Dispersion behavior of MgO, ZrO_2, Al_2O_3, CaO–Al_2O_3 and MnO–SiO_2 deoxidation particles during solidification of Fe–10mass%Ni alloy, *ISIJ Int.*, 46(2006), No. 1, p. 22.

[59] T. Furukawa, N. Saito, and K. Nakashima, Evaluation of interfacial energy between molten Fe and Fe–18% Cr–9% Ni alloy and non-metallic inclusion-type oxides, *ISIJ Int.*, 61(2021), No. 9, p. 2381.

[60] X.P. Guo, M. Tan, T. Li, *et al.*, Formation mechanisms and three-dimensional characterization of composite inclusion of MnS–Al_2O_3 in high speed wheel steel, *Mater. Charact.*, 197(2023), art. No. 112669.

[61] Y.F. Qi, J. Li, C.B. Shi, H. Wang, and D.L. Zheng, Precipitation and growth of MnS inclusion in an austenitic hot-work die steel during ESR solidification process, *Metall. Res. Technol.*, 116(2019), No. 3, art. No. 322.

[62] S.C. Duan, J. Kang, J. Cho, M. Lee, W.Z. Mu, and J.H. Park, Manufacturing an ultra-low-sulfur CoCrFeMnNi high-entropy alloy by slagging through induction melting with ferroalloys feedstock, *J. Alloys Compd.*, 928(2022), art. No. 167080.

[63] J. Zeng, C.Y. Zhu, W.L. Wang, and X. Li, *In situ* observation of the MnS precipitation behavior in high-sulfur microalloyed steel under different cooling rates, *Metall. Mater. Trans. B*, 51(2020), No. 6, p. 2522.

[64] Z.L. Xue, N. Li, L. Wang, S.Q. Song, D.M. Liu, and A. Huang, A coupling model predicting the precipitation and growth of MnS inclusions in U75V high-carbon heavy rail steel, *Metall. Mater. Trans. B*, 52(2021), No. 6, p. 3860.

[65] D.M. Liu, Z.L. Xue, and S.Q. Song, Effect of manganese on the formation mechanism of nonmetallic inclusions in Fe–xMn–7Al–0.7C lightweight steel, *Steel Res. Int.*, 94(2023), No. 1, art. No. 2200551.

[66] J.H. Shin and J.H. Park, Modification of inclusions in molten steel by Mg-Ca transfer from top slag: Experimental confirmation of the 'refractory-slag-metal-inclusion (ReSMI)' multiphase reaction model, *Metall. Mater. Trans. B*, 48(2017), No. 6, p. 2820.

[67] C.B. Shi, H. Wang, and J. Li, Effects of reoxidation of liquid steel and slag composition on the chemistry evolution of inclusions during electroslag remelting, *Metall. Mater. Trans. B*, 49(2018), No. 4, p. 1675.

[68] M.G. González-Solórzano, R. Morales, J.R. Ávila, C.R. Muñiz-Valdés, and A.N. Bastida, Alumina nucleation, growth kinetics, and morphology: A review, *Steel Res. Int.*, 94(2023), No. 9, art. No. 2200678.

[69] Q.F. Shu, V.V. Visuri, T. Alatarvas, and T. Fabritius, Model for inclusion precipitation kinetics during solidification of steel applications in MnS and TiN inclusions, *Metall. Mater. Trans. B*, 51(2020), No. 6, p. 2905.

[70] D.L. Zheng, G.J. Ma, J. Li, *et al.*, Effect of cerium on the primary carbides and inclusions in electroslag remelted M35 high speed steel, *J. Mater. Res. Technol.*, 24(2023), p. 8252.

[71] M. Yoshizawa, M. Igarashi, and T. Nishizawa, Effect of tungsten on the Ostwald ripening of $M_{23}C_6$ carbides in martensitic heat resistant steel, *Tetsu-to-Hagane*, 91(2005), No. 2, p. 272.

[72] X. Xiao, G.Q. Liu, B.F. Hu, J.S. Wang, and W.B. Ma, Coarsening behavior for M23C6 carbide in 12%Cr-reduced activation ferrite/martensite steel: Experimental study combined with DICTRA simulation, *J. Mater. Sci.*, 48(2013), No. 16, p. 5410.

[73] J.P. Sanhueza, D. Rojas, J. García, *et al.*, Computational modeling of the effect of B and W in the phase transformation of M23C6 carbides in 9 to 12 pct Cr martensitic/ferritic steels, *Mater. Res. Express*, 6(2019), No. 11, art. No. 1165d3.

[74] M.E. Fraser and A. Mitchell, Mass transfer in the electroslag process. Part1: Mass-transfer model, *Ironmaking Steelmaking*, 3(1976), No. 5, p. 279.

[75] M. Valdez, G.S. Shannon, and S. Sridhar, The ability of slags to absorb solid oxide inclusions, *ISIJ Int.*, 46(2006), No. 3, p. 450.

[76] Y. Wen, Q. Shu, Y. Lin, and T. Fabritius, Effect of SiO_2 content and mass ratio of CaO to Al_2O_3 on the viscosity and struc-

ture of $CaO–Al_2O_3–B_2O_3–SiO_2$ slags, *ISIJ Int.*, 63(2023), No. 1, p. 1.
[77] I.H. Jung and M.A. Van Ende, Computational thermodynamic calculations: FactSage from CALPHAD thermodynamic database to virtual process simulation, *Metall. Mater. Trans. B*, 51(2020), No. 5, p. 1851.
[78] C.B. Shi, S.J. Wang, J. Li, and J.W. Cho, Non-metallic inclusions in electroslag remelting: A review, *J. Iron Steel Res. Int.*, 28(2021), No. 12, p. 1483.
[79] G.K. Sigworth and J.F. Elliott, The thermodynamics of liquid dilute iron alloys, *Met. Sci.*, 8(1974), No. 1, p. 298.
[80] G.Q. Li and H. Suito, Electrochemical measurement of critical supersaturation in F–O–M (M=Al, Si, and Zr) and Fe–O–Al–M (M=C, Mn, Cr, Si, and Ti) melts by solid electrolyte galvanic cell, *ISIJ Int.*, 37(1997), No. 8, p. 762.
[81] T.S. Kim, S.B. Lee, and J.H. Park, Effect of tundish flux on compositional changes in non-metallic inclusions in stainless steel melts, *ISIJ Int.*, 61(2021), No. 12, p. 2998.
[82] M. Hino and K. Ito, *Thermodynamic Data for Steelmaking*, Tohoku University Press, Sendai, 2010, p. 259.
[83] M. Kishi, R. Inoue, and H. Suito, Thermodynamics of oxygen and nitrogen in liquid Fe-20mass%Cr alloy equilibrated with titania-based slags, *ISIJ Int.*, 34(1994), No. 11, p. 859.
[84] H. Suito and R. Inoue, Thermodynamics on control of inclusions composition in ultra-clean steels, *ISIJ Int.*, 36(1996), No. 5, p. 528.
[85] T.J. Wen, Q. Ren, L.F. Zhang, *et al.*, Evolution of nonmetallic inclusions during the electroslag remelting process, *Steel Res. Int.*, 92(2021), No. 6, art. No. 2000629.
[86] T.F. Li, G.Q. Li, Z. Zhang, Y. Liu, and X.J. Wang, Fluoride vaporization and crystallization of $CaF_2–CaO–Al_2O_3–(La_2O_3)$ slag for vacuum electroslag remelting, *Vacuum*, 196(2022), art. No. 110807.
[87] S.C. Duan and H.J. Guo, The methodology development for improving energy utilization and reducing fluoride pollution of the electroslag remelting process: A review, *Steel Res. Int.*, 91(2020), No. 7, art. No. 1900634.
[88] C. Wagner, *Thermodynamics of Alloys*, Addison-Wesley Press, Cambridge, MA, 1952, p. 47.
[89] E. Scheil, Bemerkungen zur schichtkristallbildung, *Int. J. Mater. Res.*, 34(1942), No. 3, p. 70.
[90] S.K. Choudhary and A. Ghosh, Mathematical model for prediction of composition of inclusions formed during solidification of liquid steel, *ISIJ Int.*, 49(2009), No. 12, p. 1819.
[91] D. Hou, Z.H. Jiang, Y.W. Dong, Y. Li, W. Gong, and F.B. Liu, Mass transfer model of desulfurization in the electroslag remelting process, *Metall. Mater. Trans. B*, 48(2017), No. 3, p. 1885.
[92] H.M. Wang, T.W. Zhang, H. Zhu, G.R. Li, Y.Q. Yan, and J.H. Wang, Effect of B_2O_3 on melting temperature, viscosity and desulfurization capacity of CaO-based refining flux, *ISIJ Int.*, 51(2011), No. 5, p. 702.
[93] Q.T. Zhu, J. Li, C.B. Shi, and W.T. Yu, Effect of electroslag remelting on carbides in $8Cr_{13}MoV$ martensitic stainless steel, *Int. J. Miner. Metall. Mater.*, 22(2015), No. 11, p. 1149.